

Article

Cobalt-Doped Iron Phosphate Crystal on Stainless Steel Mesh for Corrosion-Resistant Oxygen Evolution Catalyst

Jaun An ¹, Hyebin Choi ¹, Keunyoung Lee ² and Ki-Young Kwon ^{1,2,*}¹ Department of Chemistry and RIGET, Gyeongsang National University, Jinju 52828, Republic of Korea² HAP Materials, 352-407, 501, Jinju-daero, Jinju 52828, Republic of Korea

* Correspondence: kykwon@gnu.ac.kr; Tel.: +82-55-772-1493

Abstract: We report an oxygen evolution reaction (OER) catalyst prepared by the incorporation of cobalt-doped iron phosphate on stainless steel mesh (SSM) through a one-step hydrothermal method. Compared to the catalytic property of bare SSM, our OER catalyst (0.84-CoFePi) showed a 42% improvement in current density at the potential of 1.9 V vs. RHE, and the onset potential was decreased by 26.5 mV. Furthermore, the loss in current density of bulk electrolysis after 12 h in 1 M KOH (pH 14) solution and 0.0441 wt% H₂SO₄ (pH ≈ 3) containing 0.1 M NaCl solution was negligible (3.1% and 3.2%, respectively). Moreover, our cobalt-doped iron phosphate on SSM exhibits the dramatic improvement in corrosion resistance to a basic, mild acidic solution and chloride ions compared to bare SSM.

Keywords: OER; cobalt-doped iron phosphate; stainless steel mesh; corrosion resistance



Citation: An, J.; Choi, H.; Lee, K.; Kwon, K.-Y. Cobalt-Doped Iron Phosphate Crystal on Stainless Steel Mesh for Corrosion-Resistant Oxygen Evolution Catalyst. *Catalysts* **2022**, *12*, 1521. <https://doi.org/10.3390/catal12121521>

Academic Editors: Xiangjiu Guan and Shichao Zong

Received: 1 November 2022

Accepted: 24 November 2022

Published: 25 November 2022

Publisher's Note: MDPI stays neutral with regard to jurisdictional claims in published maps and institutional affiliations.



Copyright: © 2022 by the authors. Licensee MDPI, Basel, Switzerland. This article is an open access article distributed under the terms and conditions of the Creative Commons Attribution (CC BY) license (<https://creativecommons.org/licenses/by/4.0/>).

1. Introduction

Replacing fossil fuels with renewable energy can limit accelerating global warming and cater to the rapid increase in energy demand [1]. Hydrogen fuel, currently being one of the most attractive alternatives to fossil fuels, has the highest gravimetric energy density, and the only combustion byproduct of hydrogen is water [2–6]. Hydrogen can be generated by photochemical [7,8], thermochemical [9,10], and electrochemical water decomposition [11–14]. Among them, electrochemical water splitting is currently a convenient and practical method for the generation of hydrogen with high purity. Water electrolysis is accomplished with two half-reactions, those are oxygen evolution reaction (OER), and hydrogen evolution reaction (HER). Particularly, OER, involving hydrogen coupled four electron transfer is the rate-determining step of water electrolysis [15–17]. Therefore, the development of OER catalyst is intensively studied to overcome the sluggish kinetics of OER [18–25]. Stainless steel (SS) is inexpensive, conductive, and stable in basic as well as mild acidic solution [26,27]. Therefore, there has been lots of effort to apply SS as an anode material for water electrolysis [28–30]. Additionally, stainless steel mesh (SSM) has a larger surface area due to its porous structure in which fibers are woven in a grid [31,32]. However, the impact of corrosion on SSM needs to be considered in the presence of acidic fluids or chloride solution [33–36]. Therefore, attention has been focused on improving the corrosion resistance of stainless steel.

Generally, transition metal phosphates have high catalytic performance [37,38], and doping transition metals such as Co, Fe can improve the OER activity by dropping overpotential and delivering high current density [39–41]. Particularly, amorphous cobalt phosphate was reported to have excellent OER properties by the Nocera group [42–48]. Here, we fabricated an OER catalyst in which the cobalt-doped iron phosphate is incorporated on SSM. To the best of our knowledge, it is the first report of fabricating an OER catalyst through one-step hydrothermal reaction by simply immersing SSM into the aqueous solution of phosphoric acid and cobalt nitrate. During the formation of our OER

catalyst, SSM is slightly corroded by phosphoric acid, allowing iron to leach from SSM into the solution, then the insoluble salt of cobalt-doped iron phosphate precipitates on the surface of SSM. Due to the importance of leached iron concentration, we optimized the concentration of phosphoric acid for the preparation of the OER catalyst. Compared to the catalytic property of bare SSM, our OER catalyst (0.84-CoFePi) showed a 42% improvement in current density at the potential of 1.9 V vs. RHE, and the onset potential decreased by 26.5 mV (266.2 mV to 239.7 mV). Furthermore, the loss in current density after 12 h of bulk electrolysis under 0.0441 wt% H₂SO₄ containing 0.1 M NaCl solution was less than 3.2%. Moreover, our cobalt doped iron phosphate on SSM exhibits improvement in corrosion resistance to basic, mild acidic and chloride ions containing solutions compared to bare SSM.

2. Results

The SEM images of bare SSM and prepared SSMs are shown in Figure 1a–l. Figure 1a shows the SEM image of a bare SSM in which stainless steel fibers with smooth surface are woven in a grid. SSMs were corroded by hydrothermal reaction in aqueous phosphoric acid solution. Additionally, increment in acid concentration accelerated the corrosion of SSM, making the smooth surface rougher (Figure 1b–d). The corrosion resulted in reduction in fiber thickness of SSM. The measured fiber thickness of SSMs were 24.67 μm (bare SSM), 23.65 μm (SSM-0.84), 22.82 μm (SSM-2.50), and 6.63 μm (SSM-4.14) as shown in Figure 1a–d. Compared to bare SSM, the fiber thickness of SSM-0.84 and SSM-2.50 was reduced by 1.02 and 1.85 μm, respectively, by the slight corrosion (Figure 1b,c). On the other hand, SSM-4.14 shows dramatic reduction of 18.04 μm (24.67 μm to 6.63 μm) in fiber thickness (Figure 1d,m). SSM was sometimes completely dissolved by drastic corrosion in 4.14 wt% H₃PO₄ solution. Figure S1 is a picture of SSM that corroded away after the hydrothermal reaction in 4.14 wt% H₃PO₄ solution, except for the part inserted into as homemade Teflon holder. Furthermore, in 8.14 wt% H₃PO₄ solution, SSM was totally melted after hydrothermal reaction. Figure 1e–l are SEM images of 0.84-CoFePi, 2.50-CoFePi, 4.14-CoFePi, and 8.14-CoFePi. In hydrothermal reaction, the addition of cobalt nitrate to phosphoric acid aqueous solution resulted in two crucial changes on SSM. First, octahedral crystals were precipitated. Second, the corrosion of SSM was obviously reduced compared with cobalt-free SSMs. For instance, SSM-4.14 and 4.14-CoFePi were prepared under the same acid concentration. However, as shown in Figure 1d,k, the fiber thickness of SSM-4.14 (6.63 μm) is much thinner than that of 4.14-CoFePi (23.22 μm). Therefore, it is evident that cobalt nitrate inhibited the corrosion of SSM. Figure 1n is a bar graph comparing the average vertical diagonal lengths of crystals measured from the SEM image. The average crystal sizes of 0.84-CoFePi, 2.50-CoFePi, 4.14-CoFePi, and 8.14-CoFePi were 30.29 μm, 31.56 μm, 39.89 μm, and 56.19 μm, respectively, confirming that the larger crystals were synthesized at higher acid concentration.

XRD patterns of all prepared OER catalysts on SSMs including bare SSM are represented in Figure 2a. Three peaks marked with stars are from bare SSM. All XRD patterns of 0.84-CoFePi, 2.50-CoFePi, 4.14-CoFePi, and 8.14-CoFePi are identical, indicating that the same substance has been synthesized regardless of the acid concentration. The crystals synthesized on SSM are confirmed to be Fe_{2.80}(PO₄)_{1.98}O_{0.26}(OH)_{1.82}, iron phosphate oxide hydroxide (JCPDS No. 01-070-5891). Our crystal shape and XRD pattern matched well with the iron phosphate reported by Quanyi Zhou et al. [49]. The IR spectra of 0.84-CoFePi, 2.50-CoFePi, 4.14-CoFePi, 8.14-CoFePi including bare SSM are shown in Figure 2b. The IR spectra of all the prepared SSMs were very similar. The peak at 746 cm⁻¹ belongs to the stretching of P-O-P linkages [50]. Peaks at 949 cm⁻¹ and 1027 cm⁻¹ are committed to the symmetric and asymmetric stretching peaks of P-O bond, respectively [39]. Additionally, the peak from Fe-O stretching and vibration mode appeared at 567 cm⁻¹ and 480 cm⁻¹, respectively [51]. It was confirmed by IR spectrum that the crystals synthesized by hydrothermal reaction were composed of Fe, P, and O bonds. Therefore, both XRD and FT-IR

revealed that the synthesized crystal is iron phosphate oxide hydroxide. On the other hand, the XRD pattern from cobalt species (cobalt oxide or cobalt phosphate) does not appear.

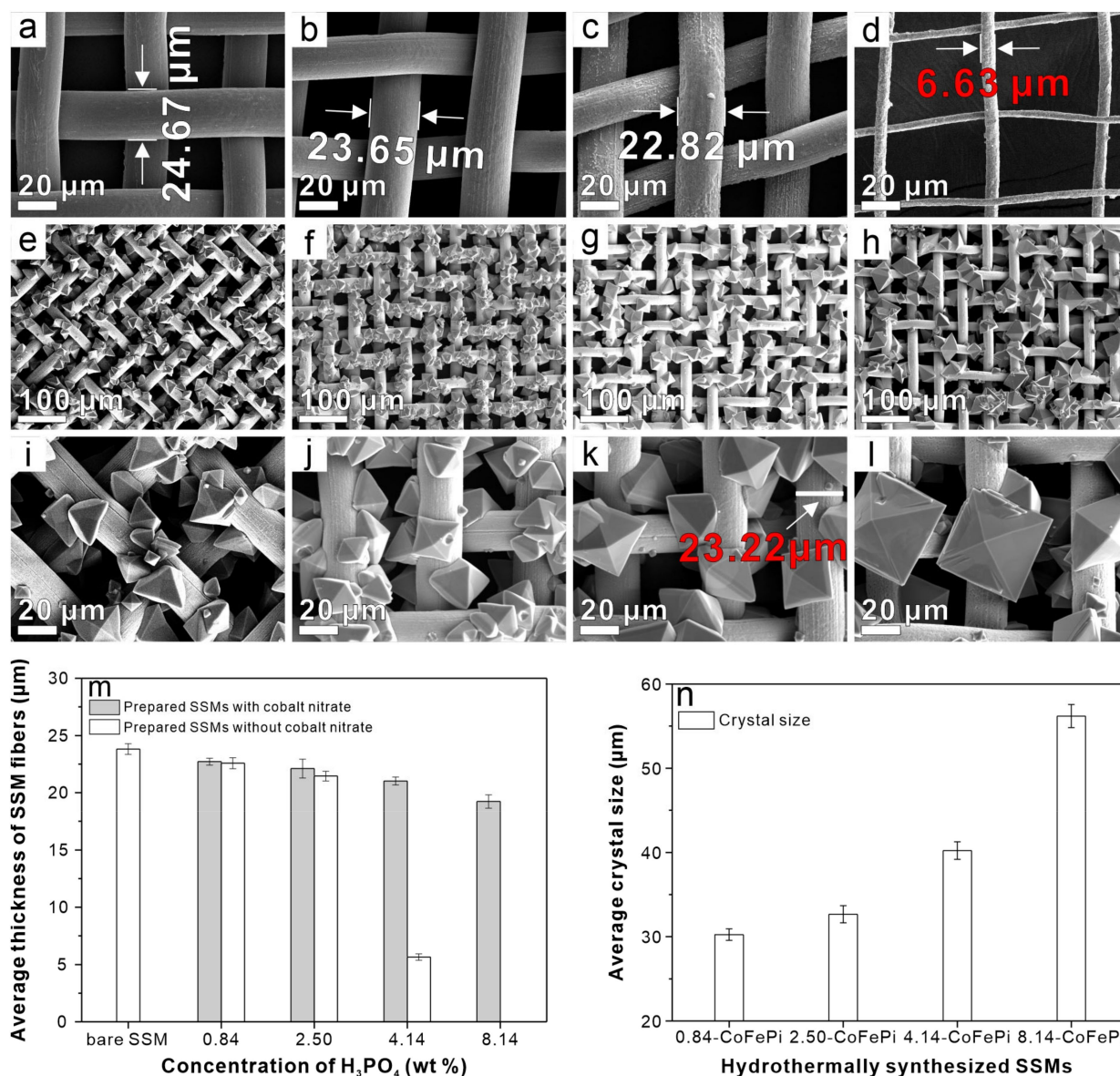


Figure 1. The SEM images of (a) bare SSM; hydrothermally synthesized SSMs under phosphoric acid aqueous solutions (b), SSM-0.84, (c) SSM-2.50, (d) SSM-4.14; SEM images of hydrothermally synthesized SSMs under cobalt nitrate and phosphoric acid aqueous solutions (e,i) 0.84-CoFePi, (f,j) 2.50-CoFePi, (g,k) 4.14-CoFePi, and (h,l) 8.14-CoFePi; (m) Average fiber thickness of prepared SSMs and (n) Crystalline size of hydrothermally synthesized crystals on SSMs.

EDS analysis was performed to investigate the element distribution of the prepared SSM. In Figure 3b–d, it was confirmed that P, O, and Co were more abundant in the crystal than the SSM substrate, indicating that the crystal is composed of phosphate anions and cobalt cations. On the other hand, Fe, Cr, and Ni are distributed more in the SSM substrate than the crystal (Figure 3e–g). Considering that the 316 SSM used in this experiment is known to be mainly composed of Fe, Cr, and Ni, it can be easily expected that the Fe, Cr, Ni will be more abundant in the substrate than the crystal.

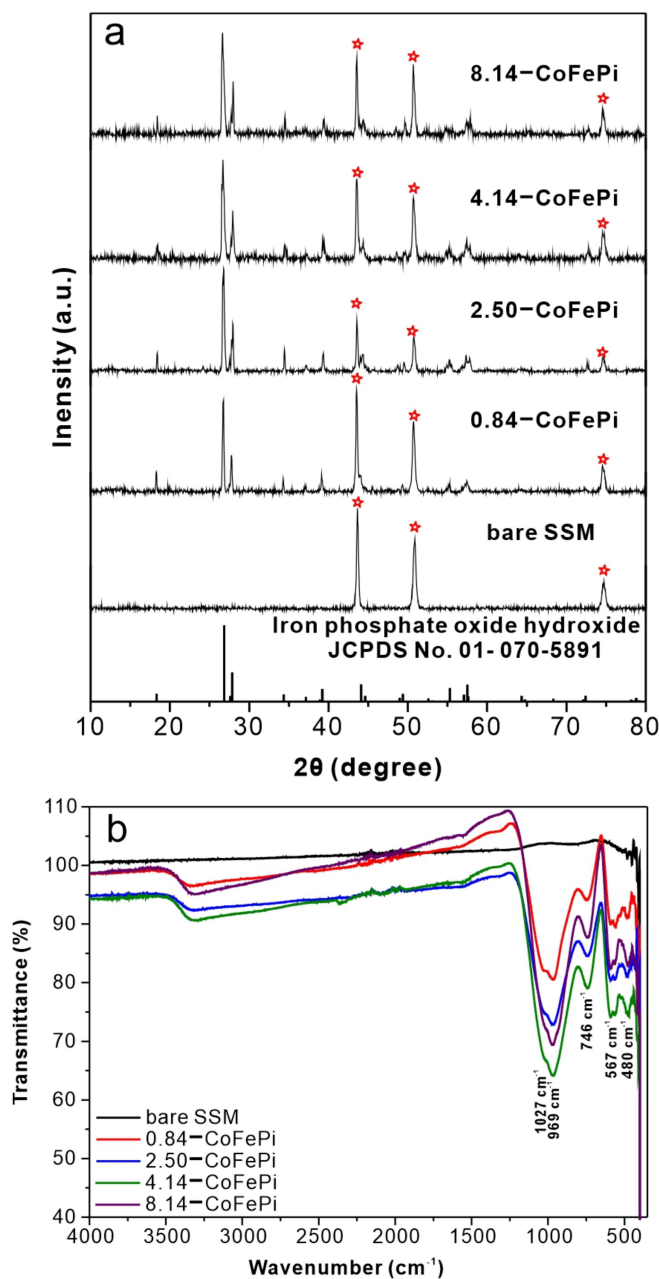


Figure 2. (a) X-ray diffraction patterns of 0.84-CoFePi, 2.50-CoFePi, 4.14-CoFePi, 8.14-CoFePi, bare SSM and iron phosphate oxide hydroxide (JCPDS No. 01-070-5891, peaks marked with red stars represent the XRD peaks from bare SSM); and (b) FT-IR spectra of 0.84-CoFePi, 2.50-CoFePi, 4.14-CoFePi, 8.14-CoFePi and bare SSM.

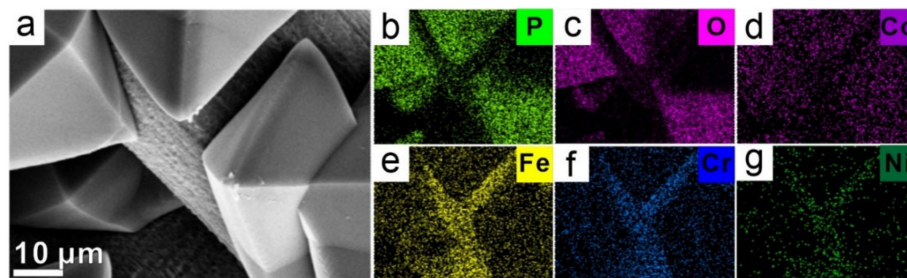


Figure 3. SEM image of (a) 0.84-CoFePi, and EDS elements mapping of 0.84-CoFePi (b) P, (c) O, (d) Co, (e) Fe, (f) Cr, and (g) Ni.

XPS analysis was performed to investigate the surface composition of 0.84-CoFePi (Figure 4). The XPS survey spectrum indicates the presence of Co, Fe, P and O (Figure 4a). Additionally, the atomic percentages of Co, Fe, P and O were 6.97%, 7.69%, 14.35%, and 69.12%, respectively. Figure 4b shows the XPS spectrum in Co 2p region, and the binding energy (BE) at 781.43 eV and 797.15 eV are assigned to be Co 2p_{3/2} and Co 2p_{1/2}, respectively [52,53]. From the deconvolution of Co 2p spectrum, peaks at the BEs of 782.71 eV and 798.74 eV are assigned to Co²⁺, while the peaks at 780.52 eV and 796.56 eV are attributed to Co³⁺ [54–57]. Furthermore, the calculated atomic ratio of the detected Co element suggests that the Co²⁺ and Co³⁺ states exist in a ratio of 6:5. In the XPS spectrum of Fe 2p region (Figure 4c), the BEs at 711.92 eV and 725.45 eV are corresponding to the peaks of Fe 2p_{3/2} and Fe 2p_{1/2}, respectively [58,59]. In addition, the deconvoluted peaks of Fe 2p at the BEs of 711.15 eV and 725.16 eV are associated with Fe²⁺, while the peaks at 713.71 eV and 728.18 eV are from Fe³⁺ [60–63]. Moreover, the atomic ratio of Fe²⁺/Fe³⁺ is 7:4. The peak in the XPS spectrum of O 1s and P 2p (Figure 4d,e) was observed with the BEs of 530.77 eV and 132.84 eV, respectively [64–67]. Therefore, from the results of XRD, FT-IR, EDS, and XPS we concluded that the crystallite is mainly composed of randomly incorporated cobalt ions on iron phosphate oxide hydroxide.

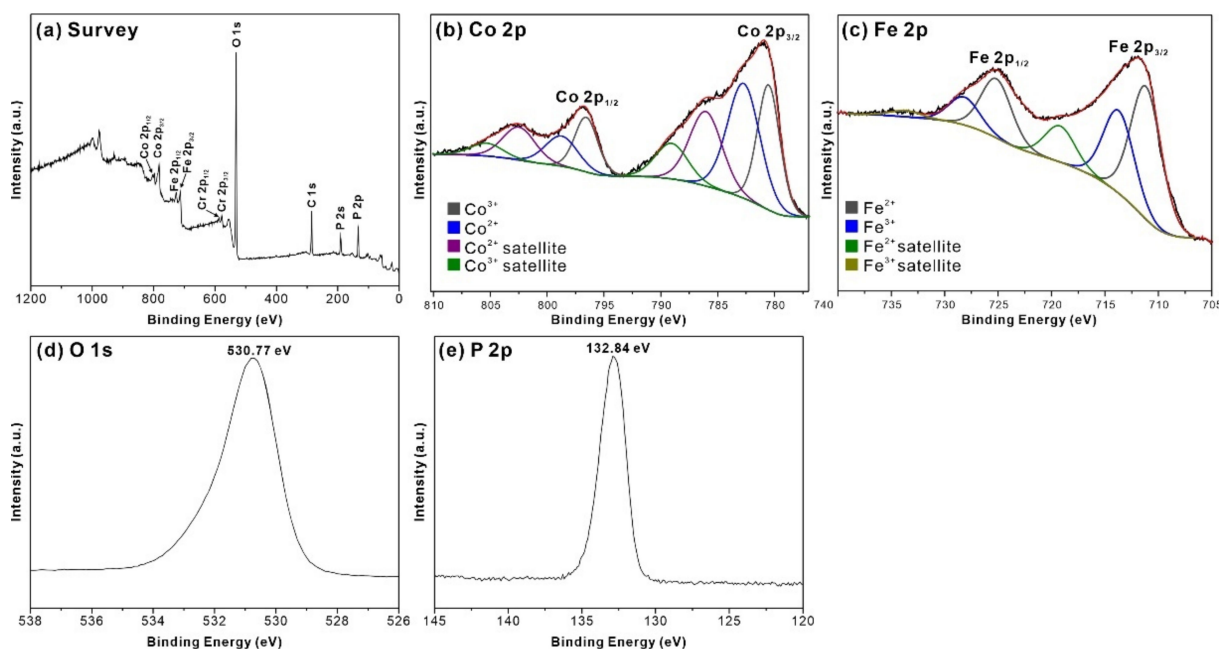


Figure 4. (a) XPS survey spectrum for iron phosphate oxide hydroxide crystal. XPS spectra of iron phosphate oxide hydroxide crystal in the (b) Co 2p, (c) Fe 2p, (d) O 1s, and (e) P 2p regions.

The evaluation in OER activity of all prepared catalysts is shown in Figure 5a–c. Polarization curves of prepared OER catalysts and bare SSM were recorded at the potential window from 1.0 V to 1.924 V vs. RHE, with the scan rate of 10 mVs^{−1} (Figure 5a). The current density at the maximum potential applied in LSV, 0.84-CoFePi showed the highest value which was increased by 42% (203.6 to 289.1 mAcm^{−2}) compared to the bare SSM. The overpotentials of all catalysts required to drive OER at 10 mAcm^{−2} were lower than bare SSM (Figure 5b). Typically, 0.84-CoFePi had the lowest overpotential of 300.3 mV, which was decreased by 31.2 mV from bare SSM (331.5 mV). The OER activity of 0.84-CoFePi was compared with recently reported Co or/and Fe based catalysts in Table S1 in Supplementary Materials. In lower acid concentration, smaller crystals precipitate on SSM, which is expected to have higher OER activities due to the larger surface area [68–72]. To evaluate the stability of the products, bulk electrolysis was carried out (Figure 5c). The average current density was 40.2 mAcm^{−2} (bare SSM), 67.8 mAcm^{−2} (0.84-CoFePi), 42.0 mAcm^{−2} (2.50-CoFePi), 38.5 mAcm^{−2} (4.14-CoFePi), and 26.2 mAcm^{−2}

(8.14-CoFePi). Compared to bare SSM, 8.14-CoFePi showed very poor OER activity, which was decreased in current density by 34.8%. However, 0.84-CoFePi showed drastic increase by 68.8% in current density. Furthermore, the loss in current density after 12 h of bulk electrolysis in 1 M KOH (pH 14) was 3.1% with better sustainability than bare SSM (11.8%).

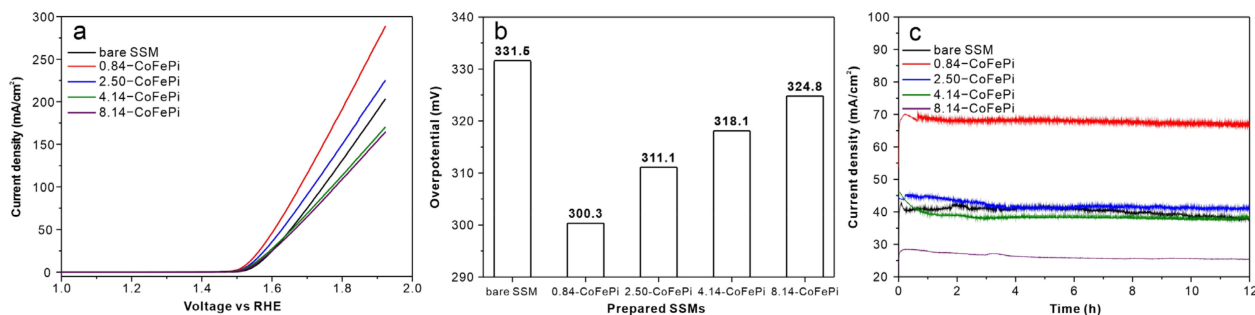


Figure 5. Electrochemical (OER) analysis of all hydrothermally synthesized OER catalysts, and bare SSM: (a) LSV curves examined with the scan rate of 10 mVs^{-1} in 1 M KOH electrolyte, (b) The overpotentials at current density of 10 mAcm^{-2} , and (c) Bulk electrolysis plotted from 12 h of hydrolysis at the voltage of 1.624 V vs. RHE in 1 M KOH electrolyte.

It is well known that the chloride ions and low pH condition accelerate corrosion of stainless steel. Li et al. reported the corrosion behavior of stainless steel by electrochemical method performed in an aqueous solution of sulfuric acid (pH 2) with different NaCl concentration. Their results suggested that chloride ions degraded the passive film of stainless steel [73]. We accomplished the bulk electrolysis of bare SSM and 0.84-CoFePi to test the stability to H_2SO_4 solution (pH \approx 3) and 0.1 M chloride ion (Figure 6b). Bare SSM was detached from sample holder due to the corrosion after 90 min of electrolysis, causing the drop in current density to zero. On the other hand, 0.84-CoFePi showed stable current density for 12 h. The loss in current density of 0.84-CoFePi after 12 h of bulk electrolysis was less than 3.2%. SEM analysis was accomplished to verify the surface morphology of bare SSM and 0.84-CoFePi (Figure 6b,c) after the bulk electrolysis. The small holes (insert of Figure 6b) appeared in bare SSM even after short OER time of 90 min, indicating that severe corrosion occurred. On the other hand, the mesh surface of 0.84-CoFePi was clean after 12 h of OER with no trace of corrosion. Therefore, our catalyst had improved durability in acidic solution compared to bare SSM. This result was predicted from the result of SEM previously discussed in Figure 1 in which the presence of cobalt species dramatically inhibits corrosion of SSM.

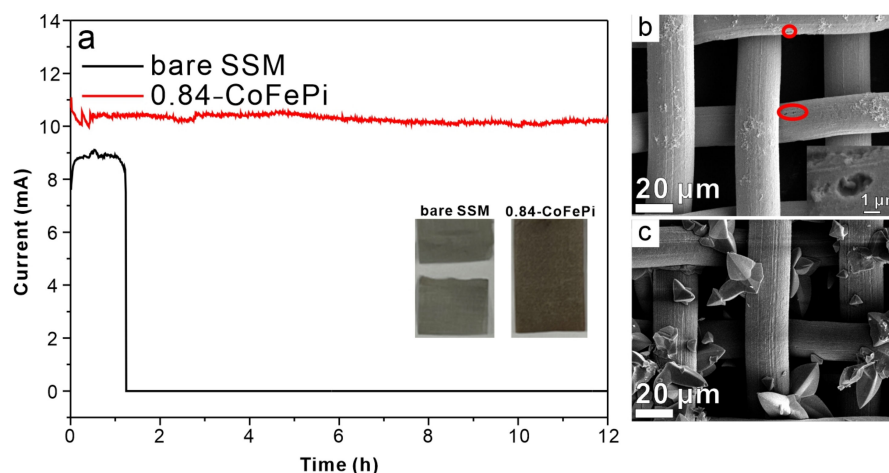


Figure 6. (a) Bulk electrolysis of bare SSM and 0.84-CoFePi in 0.0441 wt% H_2SO_4 solution containing 0.1 M NaCl at the voltage of 2.164 V vs. RHE for 12 h; SEM images of (b) bare SSM after the bulk electrolysis, and (c) 0.84-CoFePi after the bulk electrolysis.

3. Materials and Methods

3.1. Materials

Phosphoric acid (85%), sulfuric acid, cobalt nitrate hexahydrate, and acetone (99.5%) were purchased from Daejung chemicals (Siheung, Republic of Korea). Sodium chloride was purchased from Sigma Aldrich (St. Louis, MO, USA). 316 Stainless steel mesh was purchased from All for lab (Seoul, Republic of Korea). Silicon glue (3145 RTV) was purchased from Dow Corning. All chemicals were used as received without purification.

3.2. Cleaning SSMs and the Corrosion of SSM by Phosphoric Acid in Hydrothermal Treatment

Firstly, SSMs were cut into pieces (1 cm × 2 cm) and washed with hexane, acetone, and DI water under ultrasonication for 5 min, respectively. Then, SSMs were dried in 75 °C oven at ambient atmosphere and cooled naturally to room temperature. The 0.84, 2.50, 4.14 and 8.14 wt% phosphoric acid solutions were prepared by diluting 85% phosphoric acid with DI water. The cleaned SSM was vertically placed on a homemade Teflon holder and was immersed into the above prepared 20 mL of phosphoric acid solution in 50 mL Teflon lined autoclave, followed by heating in an oven at 200 °C for 12 h (denoted as SSM-0.84, SSM-2.50, SSM-4.14, and SSM-8.14, respectively). The autoclave was cooled down to room temperature, and the SSM was gently washed with 100 mL of DI water 3 times, and dried in 75 °C oven.

3.3. Preparation of OER Catalyst on SSMs

In this process, 0.4 mmol of cobalt nitrate hexahydrate was added to the 20 mL of 0.84, 2.50, 4.14 and 8.14 wt% H₃PO₄ aqueous solutions, respectively. The cleaned SSM was vertically immersed into the above prepared 20 mL of phosphoric acid and cobalt nitrate solutions in 50 mL Teflon lined autoclave, followed by heating in an oven at 200 °C for 12 h (denoted as 0.84-CoFePi, 2.50-CoFePi, 4.14-CoFePi, and 8.14-CoFePi, respectively). All subsequent processes were the same as done above.

3.4. Characterizations

The surface morphology and elemental analysis of hydrothermally treated SSMs were investigated by Field Emission Scanning Electron Microscope (FE-SEM, JSM-6700F, JEOL, Tokyo, Japan) with energy dispersive spectrometer (EDS). X-ray diffraction patterns (XRD) were collected from 3 kW Cu X-ray Diffractometer, (D8 Advance, Bruker AXS, Hamburg, Germany) in the 2θ range of 5–80°. Vibrational spectra of prepared SSMs were characterized by Fourier Transform Infrared Spectroscopy (FT-IR) using Nicolet iS5 FT-IR Spectrometer (Thermo Fisher Scientific, Waltham, MA, USA) in the wavenumber range of 400–4000 cm⁻¹. X-ray photoelectron spectroscopy (XPS) was analyzed using NEXSA G2 (Thermo Fisher Scientific, Waltham, MA, USA).

3.5. Electrochemical Measurement

All electrochemical properties of the prepared SSMs were measured by a commercial potentiostat (Zive SP1 Wonatech, Seoul, Republic of Korea) with three-electrode system under aqueous solution of 1 M KOH (pH 14) and 0.0441 wt% H₂SO₄ (pH ≈ 3). In this process, 0.1 M NaCl was used as an electrolyte for the 0.0441 wt% H₂SO₄ solution. The prepared SSMs were applied as working electrodes, Hg/HgO (basic media) and Ag/AgCl (acidic media) for reference electrode and Pt plate as a counter electrode. The geometric area of prepared SSMs were adjusted to 1 × 1 cm² by screening SSM using silicon sealant. All applied potentials vs. Hg/HgO and Ag/AgCl were converted into potential vs. reversible hydrogen electrode (RHE) using the following formula:

$$E(\text{RHE}) = E(\text{Hg}/\text{HgO}, \text{Ag}/\text{AgCl}) + 0.059 \times \text{pH} (14, \approx 3) + E^0(\text{Hg}/\text{HgO}, \text{Ag}/\text{AgCl}) \quad (1)$$

Linear sweep voltammetry (LSV) was recorded at the potential range of 1.000–1.924 V vs. RHE with the scan rate of 10 mVs⁻¹. Chronoamperometry was performed to test the sus-

tainability of prepared SSMs for 12 h at the potential of 1.624, 2.164 V vs. RHE for basic and acidic solutions, respectively. Overpotential (η) was calculated by the following equation:

$$\eta = E(\text{NHE}) + 0.059 \times \text{pH} (14, \approx 3) - 1.23 \quad (2)$$

4. Conclusions

The cobalt-doped iron phosphate on SSM was synthesized via the hydrothermal method by immersing SSM in phosphoric acid and cobalt nitrate solution. SEM images showed that the octahedral crystals were precipitated on SSM. Through the XRD, FT-IR, EDS, and XPS analysis, the octahedral crystal was confirmed to be cobalt-doped iron phosphate oxide hydroxide. Additionally, the maintained fiber thickness of SSM after hydrothermal reaction indicated that cobalt nitrate inhibited the corrosion of SSM from phosphoric acid. The improved durability of our catalyst to basic, mild acidic conditions and chloride ions is thought to be due to the amorphous cobalt oxide containing phosphate group formed on the surface of SSM, which was demonstrated by the Nocera group [42–48].

Supplementary Materials: The following supporting information can be downloaded at: <https://www.mdpi.com/article/10.3390/catal12121521/s1>, Figure S1: picture of SSM that corroded away except for the part inserted into the Teflon holder. Table S1: OER activity of 0.84-CoFePi compared with recently reported Co or/and Fe based OER catalysts. References [53,74–79] are cited in the Supplementary Materials.

Author Contributions: K.-Y.K. conceived and designed the experiments; J.A. performed the syntheses of catalysts and the examination of catalytic properties; H.C. and K.L. contributed to the scientific discussion; K.-Y.K. and J.A. All authors have read and agreed to the published version of the manuscript.

Funding: This work was supported by the Basic Science Research Program through the National Research Foundation of Korea (NRF), funded by the Ministry of Education (NRF-2022R1I1A3071407), and by the Korea Basic Science Institute (KBSI), National Research Facilities & Equipment Center (NFEC) grant funded by the Ministry of Education (2019R1A6C1010042).

Data Availability Statement: The data are contained within the article.

Conflicts of Interest: The authors declare no conflict of interest.

References

1. Hosseini, S.E.; Wahid, M.A. Hydrogen production from renewable and sustainable energy resources: Promising green energy carrier for clean development. *Renew. Sust. Energy Rev.* **2016**, *57*, 850–866. [CrossRef]
2. Zhu, J.; Hu, L.; Zhao, P.; Lee, L.Y.S.; Wong, K.-Y. Recent Advances in Electrocatalytic Hydrogen Evolution Using Nanoparticles. *Chem. Rev.* **2020**, *120*, 851–918. [CrossRef]
3. Li, Z.; Wang, X.; Wang, X.; Lin, Y.; Meng, A.; Yang, L.; Li, Q. Mn-Cd-S@amorphous-Ni₃S₂ hybrid catalyst with enhanced photocatalytic property for hydrogen production and electrocatalytic OER. *Appl. Surf. Sci.* **2019**, *491*, 799–806. [CrossRef]
4. Xie, L.; Ren, X.; Liu, Q.; Cui, G.; Ge, R.; Asiri, A.M.; Sun, X.; Zhang, Q.; Chen, L. A Ni(OH)₂-PtO₂ hybrid nanosheet array with ultralow Pt loading toward efficient and durable alkaline hydrogen evolution. *J. Mater. Chem. A* **2018**, *6*, 1967–1970. [CrossRef]
5. Zaman, S.; Huang, L.; Douka, A.I.; Yang, H.; You, B.; Xia, B.Y. Oxygen Reduction Electrocatalysts toward Practical Fuel Cells: Progress and Perspectives. *Angew. Chem. Int. Ed.* **2021**, *60*, 17832–17852. [CrossRef] [PubMed]
6. Zaman, S.; Su, Y.-Q.; Dong, C.-L.; Qi, R.; Huang, L.; Qin, Y.; Huang, Y.-C.; Li, F.-M.; You, B.; Guo, W.; et al. Scalable Molten Salt Synthesis of Platinum Alloys Planted in Metal-Nitrogen-Graphene for Efficient Oxygen Reduction. *Angew. Chem. Int. Ed.* **2022**, *61*, e202115835. [CrossRef] [PubMed]
7. Ismail, A.A.; Bahnemann, D.W. Photochemical splitting of water for hydrogen production by photocatalysis: A review. *Sol. Energy Mater. Sol. Cells* **2014**, *128*, 85–101. [CrossRef]
8. Pullen, S.; Fei, H.; Orthaber, A.; Cohen, S.M.; Ott, S. Enhanced Photochemical Hydrogen Production by a Molecular Diiron Catalyst Incorporated into a Metal-Organic Framework. *J. Am. Chem. Soc.* **2013**, *135*, 16997–17003. [CrossRef] [PubMed]
9. Steinfeld, A. Solar thermochemical production of hydrogen—A review. *Sol. Energy* **2005**, *78*, 603–615. [CrossRef]
10. Steinfeld, A. Solar hydrogen production via a two-step water-splitting thermochemical cycle based on Zn/ZnO redox reactions. *Int. J. Hydrogen Energy* **2002**, *27*, 611–619. [CrossRef]
11. Xu, X.; Su, C.; Shao, Z. Fundamental Understanding and Application of Ba_{0.5}Sr_{0.5}Co_{0.8}Fe_{0.2}O_{3- δ} Perovskite in Energy Storage and Conversion: Past, Present, and Future. *Energy Fuels* **2021**, *35*, 13585–13609. [CrossRef]

12. Feng, Y.; He, T.; Alonso-Vante, N. In situ Free-Surfactant Synthesis and ORR-Electrochemistry of Carbon-Supported Co_3S_4 and CoSe_2 Nanoparticles. *Chem. Mater.* **2008**, *20*, 26–28. [[CrossRef](#)]
13. Neyerlin, K.C.; Srivastava, R.; Yu, C.; Strasser, P. Electrochemical activity and stability of dealloyed Pt–Cu and Pt–Cu–Co electrocatalysts for the oxygen reduction reaction (ORR). *J. Power Sources* **2009**, *186*, 261–267. [[CrossRef](#)]
14. Benck, J.D.; Hellstern, T.R.; Kibsgaard, J.; Chakhranont, P.; Jaramillo, T.F. Catalyzing the Hydrogen Evolution Reaction (HER) with Molybdenum Sulfide Nanomaterials. *ACS Catal.* **2014**, *4*, 3957–3971. [[CrossRef](#)]
15. Song, J.; Wei, C.; Huang, Z.-F.; Liu, C.; Zeng, L.; Wang, X.; Xu, Z.J. A review on fundamentals for designing oxygen evolution electrocatalysts. *Chem. Soc. Rev.* **2020**, *49*, 2196–2214. [[CrossRef](#)]
16. Anantharaj, S.; Venkatesh, M.; Salunke, A.S.; Simha, T.V.S.V.; Prabu, V.; Kundu, S. High-Performance Oxygen Evolution Anode from Stainless Steel via Controlled Surface Oxidation and Cr Removal. *ACS Sustain. Chem. Eng.* **2017**, *5*, 10072–10083. [[CrossRef](#)]
17. Lodhi, M.J.K.; Deen, K.M.; Haider, W. Additively manufactured 316L stainless steel: An efficient electrocatalyst. *Int. J. Hydrogen Energy* **2019**, *44*, 24698–24704. [[CrossRef](#)]
18. Guan, D.; Zhong, J.; Xu, H.; Huang, Y.-C.; Hu, Z.; Chen, B.; Zhang, Y.; Ni, M.; Xu, X.; Zhou, W.; et al. A universal chemical-induced tensile strain tuning strategy to boost oxygen-evolving electrocatalysis on perovskite oxides. *Appl. Phys. Rev.* **2022**, *9*, 011422. [[CrossRef](#)]
19. Xu, X.; Shao, Z.; Jiang, S.P. High-Entropy Materials for Water Electrolysis. *Energy Technol.* **2022**, *10*, 2200573. [[CrossRef](#)]
20. Haase, F.T.; Rabe, A.; Schmidt, F.-P.; Herzog, A.; Jeon, H.S.; Frandsen, W.; Narangoda, P.V.; Spanos, I.; Friedel Ortega, K.; Timoshenko, J.; et al. Role of Nanoscale Inhomogeneities in Co_2FeO_4 Catalysts during the Oxygen Evolution Reaction. *J. Am. Chem. Soc.* **2022**, *144*, 12007–12019. [[CrossRef](#)]
21. Tong, Y.; Liu, J.; Wang, L.; Su, B.-J.; Wu, K.-H.; Juang, J.-Y.; Hou, F.; Yin, L.; Dou, S.X.; Liu, J.; et al. Carbon-Shielded Single-Atom Alloy Material Family for Multi-Functional Electrocatalysis. *Adv. Funct. Mater.* **2022**, *32*, 2205654. [[CrossRef](#)]
22. Zaman, S.; Wang, M.; Liu, H.; Sun, F.; Yu, Y.; Shui, J.; Chen, M.; Wang, H. Carbon-based catalyst supports for oxygen reduction in proton-exchange membrane fuel cells. *Trends Chem.* **2022**, *4*, 886–906. [[CrossRef](#)]
23. Reier, T.; Pawolek, Z.; Cherevko, S.; Bruns, M.; Jones, T.; Teschner, D.; Selve, S.; Bergmann, A.; Nong, H.N.; Schlögl, R.; et al. Molecular Insight in Structure and Activity of Highly Efficient, Low-Ir Ir–Ni Oxide Catalysts for Electrochemical Water Splitting (OER). *J. Am. Chem. Soc.* **2015**, *137*, 13031–13040. [[CrossRef](#)]
24. Jamesh, M.-I.; Sun, X. Recent progress on earth abundant electrocatalysts for oxygen evolution reaction (OER) in alkaline medium to achieve efficient water splitting—A review. *J. Power Sources* **2018**, *400*, 31–68. [[CrossRef](#)]
25. Dutta, A.; Pradhan, N. Developments of Metal Phosphides as Efficient OER Precatalysts. *J. Phys. Chem. Lett.* **2017**, *8*, 144–152. [[CrossRef](#)] [[PubMed](#)]
26. Yao, M.; Hu, H.; Wang, N.; Hu, W.; Komarneni, S. Quaternary (Fe/Ni)(P/S) mesoporous nanorods templated on stainless steel mesh lead to stable oxygen evolution reaction for over two months. *J. Colloid Interface Sci.* **2020**, *561*, 576–584. [[CrossRef](#)]
27. Nandanapalli, K.R.; Mudusu, D.; Karuppanan, R.; Hahn, Y.-B.; Lee, S. Predominantly enhanced catalytic activities of surface protected ZnO nanorods integrated stainless-steel mesh structures: A synergistic impact on oxygen evolution reaction process. *Chem. Eng. J.* **2022**, *429*, 132360. [[CrossRef](#)]
28. Chen, J.S.; Ren, J.; Shalom, M.; Fellinger, T.; Antonietti, M. Stainless Steel Mesh-Supported NiS Nanosheet Array as Highly Efficient Catalyst for Oxygen Evolution Reaction. *ACS Appl. Mater. Interfaces* **2016**, *8*, 5509–5516. [[CrossRef](#)]
29. Katkar, P.K.; Marje, S.J.; Pujari, S.S.; Khalate, S.A.; Lokhande, A.C.; Patil, U.M. Enhanced Energy Density of All-Solid-State Asymmetric Supercapacitors Based on Morphologically Tuned Hydrous Cobalt Phosphate Electrode as Cathode Material. *ACS Sustain. Chem. Eng.* **2019**, *7*, 11205–11218. [[CrossRef](#)]
30. Zhang, Q.; Zhong, H.; Meng, F.; Bao, D.; Zhang, X.; Wei, X. Three-dimensional interconnected $\text{Ni}(\text{Fe})\text{O}_x\text{H}_y$ nanosheets on stainless steel mesh as a robust integrated oxygen evolution electrode. *Nano Res.* **2018**, *11*, 1294–1300. [[CrossRef](#)]
31. Jung, S.; Yong, K. Fabrication of CuO–ZnO nanowires on a stainless steel mesh for highly efficient photocatalytic applications. *Chem. Commun.* **2011**, *47*, 2643–2645. [[CrossRef](#)]
32. Zhang, Y.; Merrill, M.D.; Logan, B.E. The use and optimization of stainless steel mesh cathodes in microbial electrolysis cells. *Int. J. Hydrogen. Energy* **2010**, *35*, 12020–12028. [[CrossRef](#)]
33. Karafyllis, G.; Galloway, A.; Humphries, E. The effect of low pH in erosion-corrosion resistance of high chromium cast irons and stainless steels. *Wear* **2019**, *420–421*, 79–86. [[CrossRef](#)]
34. Malik, A.U.; Ahmad, S.; Andijani, I.; Al-Fouzan, S. Corrosion behavior of steels in Gulf seawater environment. *Desalination* **1999**, *123*, 205–213. [[CrossRef](#)]
35. Nishimura, R. The effect of chloride ions on stress corrosion cracking of type 304 and type 316 austenitic stainless steels in sulfuric acid solution. *Corros. Sci.* **1993**, *34*, 1859–1868. [[CrossRef](#)]
36. Nishimura, R. Characterization and perspective of stress corrosion cracking of austenitic stainless steels (type 304 and type 316) in acid solutions using constant load method. *Corros. Sci.* **2007**, *49*, 81–91. [[CrossRef](#)]
37. Khalate, S.A.; Kadam, S.A.; Ma, Y.-R.; Pujari, S.S.; Marje, S.J.; Katkar, P.K.; Lokhande, A.C.; Patil, U.M. Hydrothermally synthesized Iron Phosphate Hydroxide thin film electrocatalyst for electrochemical water splitting. *Electrochim. Acta* **2019**, *319*, 118–128. [[CrossRef](#)]
38. Guo, R.; Lai, X.; Huang, J.; Du, X.; Yan, Y.; Sun, Y.; Zou, G.; Xiong, J. Phosphate-Based Electrocatalysts for Water Splitting: Recent Progress. *ChemElectroChem* **2018**, *5*, 3822–3834. [[CrossRef](#)]

39. Khalate, S.A.; Kadam, S.A.; Ma, Y.-R.; Pujari, S.S.; Patil, U.M. Cobalt doped iron phosphate thin film: An effective catalyst for electrochemical water splitting. *J. Alloys Compd.* **2021**, *885*, 160914. [[CrossRef](#)]
40. Trotochaud, L.; Young, S.L.; Ranney, J.K.; Boettcher, S.W. Nickel–Iron Oxyhydroxide Oxygen-Evolution Electrocatalysts: The Role of Intentional and Incidental Iron Incorporation. *J. Am. Chem. Soc.* **2014**, *136*, 6744–6753. [[CrossRef](#)]
41. Corrigan, D.A. The Catalysis of the Oxygen Evolution Reaction by Iron Impurities in Thin Film Nickel Oxide Electrodes. *J. Electrochem. Soc.* **1987**, *134*, 377. [[CrossRef](#)]
42. Kanan, M.W.; Nocera, D.G. In Situ Formation of an Oxygen-Evolving Catalyst in Neutral Water Containing Phosphate and Co^{2+} . *Science* **2008**, *321*, 1072–1075. [[CrossRef](#)]
43. Surendranath, Y.; Kanan, M.W.; Nocera, D.G. Mechanistic Studies of the Oxygen Evolution Reaction by a Cobalt-Phosphate Catalyst at Neutral pH. *J. Am. Chem. Soc.* **2010**, *132*, 16501–16509. [[CrossRef](#)] [[PubMed](#)]
44. Esswein, A.J.; Surendranath, Y.; Reece, S.Y.; Nocera, D.G. Highly active cobalt phosphate and borate based oxygen evolving catalysts operating in neutral and natural waters. *Energy Environ. Sci.* **2011**, *4*, 499–504. [[CrossRef](#)]
45. Kanan, M.W.; Yano, J.; Surendranath, Y.; Dincă, M.; Yachandra, V.K.; Nocera, D.G. Structure and Valency of a Cobalt–Phosphate Water Oxidation Catalyst Determined by in Situ X-ray Spectroscopy. *J. Am. Chem. Soc.* **2010**, *132*, 13692–13701. [[CrossRef](#)]
46. Kanan, M.W.; Surendranath, Y.; Nocera, D.G. Cobalt–phosphate oxygen-evolving compound. *Chem. Soc. Rev.* **2009**, *38*, 109–114. [[CrossRef](#)] [[PubMed](#)]
47. Surendranath, Y.; Dincă, M.; Nocera, D.G. Electrolyte-Dependent Electrosynthesis and Activity of Cobalt-Based Water Oxidation Catalysts. *J. Am. Chem. Soc.* **2009**, *131*, 2615–2620. [[CrossRef](#)]
48. Brodsky, C.N.; Bediako, D.K.; Shi, C.; Keane, T.P.; Costentin, C.; Billinge, S.J.L.; Nocera, D.G. Proton–Electron Conductivity in Thin Films of a Cobalt–Oxygen Evolving Catalyst. *ACS Appl. Energy Mater.* **2019**, *2*, 3–12. [[CrossRef](#)]
49. Zhou, Q.; Ni, Y.; Ni, H.; Ma, X.; Zhou, Y. Octahedral iron phosphate hydroxide microcrystals: Fast microwave-hydrothermal preparation, influencing factors and the shape evolution. *Mater. Res. Bull.* **2012**, *47*, 2464–2468. [[CrossRef](#)]
50. Shi, M.; Liang, Y.; Chai, L.; Min, X.; Zhao, Z.; Yang, S. Raman and FTIR spectra of modified iron phosphate glasses containing arsenic. *J. Mol. Struct.* **2015**, *1081*, 389–394. [[CrossRef](#)]
51. Wang, F.; Qin, X.F.; Meng, Y.F.; Guo, Z.L.; Yang, L.X.; Ming, Y.F. Hydrothermal synthesis and characterization of $\alpha\text{-Fe}_2\text{O}_3$ nanoparticles. *Mater. Sci. Semicond. Process* **2013**, *16*, 802–806. [[CrossRef](#)]
52. Wang, D.; Wang, Y.; Fu, Z.; Xu, Y.; Yang, L.-X.; Wang, F.; Guo, X.; Sun, W.; Yang, Z.-L. Cobalt–Nickel Phosphate Composites for the All-Phosphate Asymmetric Supercapacitor and Oxygen Evolution Reaction. *ACS Appl. Mater. Interfaces* **2021**, *13*, 34507–34517. [[CrossRef](#)] [[PubMed](#)]
53. Gong, L.; Chng, X.Y.E.; Du, Y.; Xi, S.; Yeo, B.S. Enhanced Catalysis of the Electrochemical Oxygen Evolution Reaction by Iron(III) Ions Adsorbed on Amorphous Cobalt Oxide. *ACS Catal.* **2018**, *8*, 807–814. [[CrossRef](#)]
54. Zhou, J.; Ge, T.; Cui, X.; Lv, J.; Guo, H.; Hua, Z.; Shi, J. A Highly Efficient Co_3O_4 Nanoparticle-Incorporated Mesoporous Beta Composite as a Synergistic Catalyst for Oxygen Reduction. *ChemElectroChem* **2017**, *4*, 1279–1286. [[CrossRef](#)]
55. Casella, I.G.; Guascito, M.R. Anodic electrodeposition of conducting cobalt oxyhydroxide films on a gold surface. XPS study and electrochemical behaviour in neutral and alkaline solution. *J. Electroanal. Chem* **1999**, *476*, 54–63. [[CrossRef](#)]
56. Khassin, A.A.; Yurieva, T.M.; Kaichev, V.V.; Bukhtiyarov, V.I.; Budneva, A.A.; Paukshtis, E.A.; Parmon, V.N. Metal–support interactions in cobalt-aluminum co-precipitated catalysts: XPS and CO adsorption studies. *J. Mol. Catal. A Chem.* **2001**, *175*, 189–204. [[CrossRef](#)]
57. Ge, L.; Han, C.; Xiao, X.; Guo, L. In situ synthesis of cobalt–phosphate (Co–Pi) modified $\text{g-C}_3\text{N}_4$ photocatalysts with enhanced photocatalytic activities. *Appl. Catal. B Environ.* **2013**, *142–143*, 414–422. [[CrossRef](#)]
58. Zhan, Y.; Lu, M.; Yang, S.; Xu, C.; Liu, Z.; Lee, J.Y. Activity of Transition-Metal (Manganese, Iron, Cobalt, and Nickel) Phosphates for Oxygen Electrocatalysis in Alkaline Solution. *ChemCatChem* **2016**, *8*, 372–379. [[CrossRef](#)]
59. Li, Y.; Zhao, C. Iron-Doped Nickel Phosphate as Synergistic Electrocatalyst for Water Oxidation. *Chem. Mater.* **2016**, *28*, 5659–5666. [[CrossRef](#)]
60. Koo, C.; Hong, H.; Im, P.W.; Kim, H.; Lee, C.; Jin, X.; Yan, B.; Lee, W.; Im, H.-J.; Paek, S.H.; et al. Magnetic and near-infrared derived heating characteristics of dimercaptosuccinic acid coated uniform $\text{Fe@Fe}_3\text{O}_4$ core–shell nanoparticles. *Nano Converg.* **2020**, *7*, 20. [[CrossRef](#)]
61. Qiao, S.; Huang, N.; Zhang, J.; Zhang, Y.; Sun, Y.; Gao, Z. Microwave-assisted synthesis of Fe-doped NiMnO_3 as electrode material for high-performance supercapacitors. *J. Solid State Electrochem.* **2019**, *23*, 63–72. [[CrossRef](#)]
62. Samuel, E.; Joshi, B.; Jo, H.S.; Kim, Y.I.; An, S.; Swihart, M.T.; Yun, J.M.; Kim, K.H.; Yoon, S.S. Carbon nanofibers decorated with FeOx nanoparticles as a flexible electrode material for symmetric supercapacitors. *Chem. Eng. J.* **2017**, *328*, 776–784. [[CrossRef](#)]
63. Ramírez-Sánchez, I.M.; Bandala, E.R. Photocatalytic Degradation of Estriol Using Iron-Doped TiO_2 under High and Low UV Irradiation. *Catalysts* **2018**, *8*, 625. [[CrossRef](#)]
64. Qian, X.; Qin, H.; Meng, T.; Lin, Y.; Ma, Z. Metal Phosphate-Supported Pt Catalysts for CO Oxidation. *Materials* **2014**, *7*, 8105–8130. [[CrossRef](#)] [[PubMed](#)]
65. Ahn, H.S.; Tilley, T.D. Electrocatalytic Water Oxidation at Neutral pH by a Nanostructured $\text{Co}(\text{PO}_3)_2$ Anode. *Adv. Funct. Mater.* **2013**, *23*, 227–233. [[CrossRef](#)]

66. Lee, R.-L.; Tran, P.D.; Pramana, S.S.; Chiam, S.Y.; Ren, Y.; Meng, S.; Wong, L.H.; Barber, J. Assembling graphitic-carbon-nitride with cobalt-oxide-phosphate to construct an efficient hybrid photocatalyst for water splitting application. *Catal. Sci. Technol.* **2013**, *3*, 1694–1698. [[CrossRef](#)]
67. Xie, L.; Zhang, R.; Cui, L.; Liu, D.; Hao, S.; Ma, Y.; Du, G.; Asiri, A.M.; Sun, X. High-Performance Electrolytic Oxygen Evolution in Neutral Media Catalyzed by a Cobalt Phosphate Nanoarray. *Angew. Chem. Int. Ed.* **2017**, *56*, 1064–1068. [[CrossRef](#)]
68. Du, J.; Shi, X.; Shan, Y.; Wang, Y.; Zhang, W.; Yu, Y.; Shan, W.; He, H. The effect of crystallite size on low-temperature hydrothermal stability of Cu-SAPO-34. *Catal. Sci. Technol.* **2020**, *10*, 2855–2863. [[CrossRef](#)]
69. Wang, Z.; Zhang, R.; Yan, X.; Fan, K. Structure and activity of nanozymes: Inspirations for de novo design of nanozymes. *Mater. Today* **2020**, *41*, 81–119. [[CrossRef](#)]
70. Seo, B.; Sa, Y.J.; Woo, J.; Kwon, K.; Park, J.; Shin, T.J.; Jeong, H.Y.; Joo, S.H. Size-Dependent Activity Trends Combined with in Situ X-ray Absorption Spectroscopy Reveal Insights into Cobalt Oxide/Carbon Nanotube-Catalyzed Bifunctional Oxygen Electrocatalysis. *ACS Catal.* **2016**, *6*, 4347–4355. [[CrossRef](#)]
71. Kim, D.S.; Han, S.J.; Kwak, S.-Y. Synthesis and photocatalytic activity of mesoporous TiO₂ with the surface area, crystallite size, and pore size. *J. Colloid Interface Sci.* **2007**, *316*, 85–91. [[CrossRef](#)] [[PubMed](#)]
72. Liang, C.; Cheong, J.Y.; Sitaru, G.; Rosenfeldt, S.; Schenk, A.S.; Gekle, S.; Kim, I.I.D.; Greiner, A. Size-Dependent Catalytic Behavior of Gold Nanoparticles. *Adv. Mater. Interfaces* **2022**, *9*, 2100867. [[CrossRef](#)]
73. Li, D.G.; Wang, J.D.; Chen, D.R.; Liang, P. Influences of pH value, temperature, chloride ions and sulfide ions on the corrosion behaviors of 316L stainless steel in the simulated cathodic environment of proton exchange membrane fuel cell. *J. Power Sources* **2014**, *272*, 448–456. [[CrossRef](#)]
74. Balram, A.; Zhang, H.; Santhanagopalan, S. Enhanced Oxygen Evolution Reaction Electrocatalysis via Electrodeposited Amorphous α -Phase Nickel-Cobalt Hydroxide Nanodendrite Forests. *ACS Appl. Mater. Interfaces* **2017**, *9*, 28355–28365. [[CrossRef](#)] [[PubMed](#)]
75. Masa, J.; Xia, W.; Sinev, I.; Zhao, A.; Sun, Z.; Grützke, S.; Weide, P.; Muhler, M.; Schuhmann, W. Mn_xO_y/NC and Co_xO_y/NC Nanoparticles Embedded in a Nitrogen-Doped Carbon Matrix for High-Performance Bifunctional Oxygen Electrodes. *Angew. Chem. Int. Ed.* **2014**, *53*, 8508–8512. [[CrossRef](#)]
76. Xu, L.; Jiang, Q.; Xiao, Z.; Li, X.; Huo, J.; Wang, S.; Dai, L. Plasma-Engraved Co₃O₄ Nanosheets with Oxygen Vacancies and High Surface Area for the Oxygen Evolution Reaction. *Angew. Chem. Int. Ed.* **2016**, *55*, 5277–5281. [[CrossRef](#)]
77. Bao, J.; Xie, J.; Lei, F.; Wang, Z.; Liu, W.; Xu, L.; Guan, M.; Zhao, Y.; Li, H. Two-Dimensional Mn-Co LDH/Graphene Composite towards High-Performance Water Splitting. *Catalysts* **2018**, *8*, 350. [[CrossRef](#)]
78. Gao, L.; Chang, S.; Zhang, Z. High-Quality CoFeP Nanocrystal/N, P Dual-Doped Carbon Composite as a Novel Bifunctional Electrocatalyst for Rechargeable Zn–Air Battery. *ACS Appl. Mater. Interfaces* **2021**, *13*, 22282–22291. [[CrossRef](#)]
79. Ao, K.; Daoud, W.A. Facile controlled formation of CoNi alloy and CoO embedded in N-doped carbon as advanced electrocatalysts for oxygen evolution and zinc-air battery. *Electrochim. Acta* **2021**, *395*, 139204. [[CrossRef](#)]